## PAPER

Check for updates

# Development of PdO/Sr₃Fe₂O₇₋δ/α-Al₂O₃ catalysts for methane combustion†

Yeon-Bin Choi,‡§[a] Tae Wook Kang,‡[a] Seo Young Kim,[a] Seon Tae Kim,[a] Byungseo Bae, [b] Do Yun Kim,*[c] Jin-Su Kwak*[c] and Sun Woog Kim [*a]

Catalysts, consisting of palladium supported on Ruddlesden–Popper (RP) type Sr₃Fe₂O₇₋δ perovskite oxides, were synthesized using co-precipitation and impregnation methods for efficient methane combustion at low temperatures. Achieving effective and stable methane combustion over Sr₃Fe₂O₇₋δ perovskite-based catalysts necessitates the suppression of the transformation of the RP-type Sr₃Fe₂O₇₋δ perovskite structure supporting active Pd species and the thermal reaction process. In this study, we demonstrated that the use of α-Al₂O₃ as a supporting material in PdO/Sr₃Fe₂O₇₋δ/α-Al₂O₃ catalysts significantly improved the surface oxygen species and oxygen vacancy density as well as the structural stability of the composite oxide catalyst. Among the catalysts prepared, the 13 wt% PdO/16 wt% Sr₃Fe₂O₇₋δ/α-Al₂O₃ catalyst exhibited the highest catalytic activity for complete methane combustion at a low temperature of 300 °C.

## Introduction

Methane (CH₄) represents one of the cleanest fossil fuel sources and holds great potential in achieving carbon neutrality.[1–3] It serves as the primary component in natural gas, shale gas, and coal-bed gas, with broad applications as an alternative to crude oil in various sectors such as ships, motor vehicles, power stations, and more.[4–7] However, the detrimental impact of unburnt CH₄ emissions is a pressing concern due to CH₄'s significantly higher global warming potential (at least seventy-two times greater than CO₂), contributing to the ongoing greenhouse effect.[8,9] Thus, the widespread adoption of LNG-powered ships and LNG power plants is essential to curb methane emissions.[10–12]

Catalytic combustion has emerged as an effective method for mitigating these emissions by enabling CH₄ oxidation at low temperatures, producing only water vapor and carbon dioxide with minimal NO$_x$ and CO emissions.[13–20] Nonetheless, CH₄, with its stable tetrahedral structure, is challenging to activate

and oxidize under mild conditions. While Pd-supported CeO₂–ZrO₂ catalysts have been commonly used for methane combustion, they are sensitive to water vapor, which can hinder combustion and catalytic performance.[21–25] Moreover, CeO₂-based catalysts contain rare earth elements, making them economically challenging to produce.[26] In addition, it has been reported that the complete combustion of methane for the catalyst systems loaded with Pd occurred at a high temperature over 400 °C under the conditions of high methane concentration over 1 vol% and low Pd loading amount under 4 wt%, as summarized in Table S1.† In order to realize the complete combustion of methane and further lower the temperature under these harsh conditions, it is necessary to develop a novel catalyst loaded with Pd.

To address these challenges, we aim to develop high-activity catalysts that facilitate CH₄ combustion at low temperatures, reduce the activation energy for oxygen migration, and enhance water resistance.[27,28] Among perovskite catalysts, Sr–Fe-based perovskite-type oxides, following the Mars–van Krevelen (MvK)-type mechanism,[29–35] are promising for CH₄ oxidation at moderate temperatures. Additionally, Ruddlesden–Popper (RP)-type layered perovskite oxides, such as Sr₃Fe₂O₇₋δ, offer unique electron and ion transport properties.[36–39] The RP-type structure of Sr₃Fe₂O₇₋δ exhibits high oxygen migration capability,[40–46] making it a suitable candidate for low-temperature methane combustion. The oxygen vacancy defects formed through the electron transition of Fe⁴⁺ → Fe³⁺ can enhance the oxygen mobility in the crystal lattice, thereby contributing to increased methane decomposition efficiency of the catalysts.[47–49] However, to serve as an effective catalyst, Sr₃Fe₂O₇₋δ needs structural stability, water resistance, and high oxygen storage and release

[a]Electronic Convergence Materials Division, Optic & Electronic Component Materials Center, Korea Institute of Ceramic Engineering and Technology, Jinju 52851, Republic of Korea. E-mail: skim80@kicet.re.kr

[b]Advanced Resources Team, Yeongwol Industrial Promotion Agency, 21–28 Palgoe 1 Nonggongdanji, Yeongwolgun 26240, Republic of Korea

[c]HD Korea Shipbuilding & Offshore Engineering Co., Ltd, 477 Bundangsuseo-ro, Bundang-gu, Seongnam-si, Gyeonggi-do 13591, Republic of Korea. E-mail: doyun.kim@ksoe.co.kr

† Electronic supplementary information (ESI) available. See DOI: https://doi.org/10.1039/d5ra02851e

‡ These authors contributed equally to this work.

§ Current address: Advanced Resources Team, Yeongwol Industrial Promotion Agency, 21–28 Palgoe 1 Nonggongdanji, Yeongwolgun 26240, Republic of Korea.
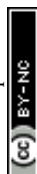
ability. While $\gamma$-Al$_2$O$_3$ is a common support for methane combustion catalysts due to its high specific surface area, it promotes unwanted reactions with water and lowers catalytic activity.[50–52] In contrast, $\alpha$-Al$_2$O$_3$ has weaker interactions with Pd species, high thermal stability, superior water resistance, and a lower specific surface area.[53] In view of the above, this study focuses on using RP-type Sr$_3$Fe$_2$O$_{7-\delta}$ perovskite oxide as a catalyst promoter for low-temperature methane combustion, supported by $\alpha$-Al$_2$O$_3$ to enhance structural stability without forming Pd–O–Al bonds. The investigation includes the influence of the $\alpha$-Al$_2$O$_3$ support on the catalyst and the methane oxidation performance of the resulting catalyst, considering oxygen storage and release ability, perovskite structure effects, and the role of the $\alpha$-Al$_2$O$_3$ support.

# Experimental

## Material

Strontium nitrate (Sr(NO$_3$)$_2$, $\geq$98%) were guaranteed reagents from Daejung Chemicals & Metals Co. Ltd. Iron(III) nitrate nonahydrate (Fe(NO$_3$)$_3$·9H$_2$O, $\geq$98%) was purchased from SIGMA-ALDRICH. 1 N-Potassium hydroxide standard solution (5–6%) was from Daejung Chemicals & Metals Co. Ltd. $\gamma$-Al$_2$O$_3$ powder (99.997%) were from Alfa Aesar. The physical properties, BET surface area (m$^2$ g$^{-1}$), and particle size ($\mu$m) of $\gamma$-Al$_2$O$_3$ were about 210, and 1–5, respectively. The core elements for oxidation of CH$_4$ commercially Pd catalysts (<20% loading) were used from conversion of Palladium (II) nitrate hydrate (Pd(NO$_3$)$_2$, 37–42%, SIGMA-ALDRICH) to PdO by impregnation method.

## Synthesis of Sr$_3$Fe$_2$O$_{7-\delta}$-based complex oxide catalysts

The Sr$_3$Fe$_2$O$_{7-\delta}$/$\alpha$-Al$_2$O$_3$ catalyst was prepared using a co-precipitation process. $\gamma$-Al$_2$O$_3$ powder (0.4 g, 99.997%, Alfa Aesar) was suspended in 1.0 mol L$^{-1}$ Sr(NO$_3$)$_2$ aq. and 1.0 mol L$^{-1}$ Fe(NO$_3$)$_3$ aq. in the stoichiometric ratio. The loading amount of Sr$_3$Fe$_2$O$_{7-\delta}$ was adjusted to be 16wt% by using 0.46 mL of 1.0 mol L$^{-1}$ Sr(NO$_3$)$_2$ aq. and 0.31 mL of 1.0 mol L$^{-1}$ Fe(NO$_3$)$_3$ aq., respectively. After stirring at room temperature for 30 minutes, the pH of the solution was adjusted to 13.6 by adding 5 vol% KOH aqueous solution drop by drop, followed by further stirring at room temperature for 6 hours. The resulting product was collected by filtration, dried at 80 °C for 12 hours, and calcined at 1000 °C for 12 hours under ambient atmosphere to obtain the 16wt% Sr$_3$Fe$_2$O$_{7-\delta}$/$\alpha$-Al$_2$O$_3$ catalysts. For comparison, Sr$_3$Fe$_2$O$_7$ catalyst also synthesized as with the previous method.

PdO was loaded onto 16wt%Sr$_3$Fe$_2$O$_{7-\delta}$/$\alpha$-Al$_2$O$_3$ via the impregnation method. The 16wt%Sr$_3$Fe$_2$O$_{7-\delta}$/$\alpha$-Al$_2$O$_3$ catalyst was impregnated with PdO by suspending the catalyst powder (0.4 g) in 1.0 mol L$^{-1}$ Pd(NO$_3$)$_2$ aq. (Sigma Aldrich), followed by adding 30 mL of deionized water. PdO loading ranged from 0 to 20 wt%. The mixture was stirred at room temperature for 6 hours, and then the solvent was evaporated at 180 °C. The residue was ground and calcined at 400 °C for 4 hours under atmospheric pressure to produce the corresponding $\alpha$wt%PdO/

16wt%Sr$_3$Fe$_2$O$_{7-\delta}$/$\alpha$-Al$_2$O$_3$ catalysts (0 $\leq \alpha \leq$ 20). For comparison, 10wt%PdO/Sr$_3$Fe$_2$O$_{7-\delta}$ and 10wt%PdO/$\alpha$-Al$_2$O$_3$ catalysts were also synthesized, in which 10wt%PdO/Sr$_3$Fe$_2$O$_{7-\delta}$ and 10wt%PdO/$\alpha$-Al$_2$O$_3$ catalyst (using $\alpha$-Al$_2$O$_3$ powder, 98%, DAE-JUNG) were calcined at 400 °C for 4 hours.

## Catalyst characterization

The crystalline phase of the catalysts was identified by X-ray powder diffraction (XRD, Bruker D8 Advance) using Cu-K$\alpha$ radiation (40 kV, 40 mA) in the $2\theta$ range of 10–80° with a step size of 0.02° and a scan speed of 0.2°·min$^{-1}$. The chemical composition of the samples was determined by inductively coupled plasma optical emission spectrometer (ICP-OES, Varian 720-ES). The crystallographic parameters were refined via Rietveld refinement (RIETAN-FP). In the refinement, the crystallographic parameters of Sr$_3$Fe$_2$O$_7$ were obtained from the inorganic crystal structure data (Sr$_3$Fe$_2$O$_7$: ICSD #74422) and were used as the starting model for refinement. The crystallite size was calculated from the measured XRD peak data using Scherrer's equation. The microstructure of the samples is observed by Cs-corrector transmission electron microscope (Cs-TEM, FEI ThemisZ) with energy-dispersive X-ray spectroscopy (EDS). The distribution of elements in the catalyst was measured by Cs-TEM with a back-scattered electron detector. The Brunauer–Emmett–Teller (BET) specific surface areas were measured at −196 °C through N$_2$ adsorption (TriStar 3020, Shimadzu). The acidity and basicity were evaluated using the temperature-programmed desorption method using ammonia and carbon dioxide (NH$_3$-TPD/CO$_2$-TPD, Micromeritics AutoChem II 2920 Chemisorption Analyzer). After preheating the sample (0.1 g) at 500 °C for 1 h under a flow of helium gas (50 mL min$^{-1}$), the sample was exposed to ammonia (10 vol% NH$_3$/90 vol% He, 50 mL min$^{-1}$) and carbon dioxide (10 vol% CO$_2$/90 vol% He, 50 mL min$^{-1}$) at 50 °C for 30 min, followed by purging at the same temperature for 15 min under helium flow (50 mL min$^{-1}$). Subsequently, the temperature was increased at a rate of 10 °C min$^{-1}$ under helium flow at a rate of 30 mL min$^{-1}$ (BELCAT-B, Microtrac BEL). H$_2$-temperature programmed reduction (H$_2$-TPR) was conducted under 5 vol% H$_2$/95 vol% Ar gas flow (50 mL min$^{-1}$) at a heating rate of 5 °C min$^{-1}$ (Micromeritics Auto Chem II 2920 Chemisorption Analyzer). Subsequently, the oxygen storage capacity (OSC) was investigated using the reduced sample after preheating under 5 vol% O$_2$/95 vol% H$_2$ gas flow (50 mL min$^{-1}$) at a heating rate of 5 °C min$^{-1}$, by means of the pulse-injection method at 500 °C (Micromeritics Auto Chem II 2920 Chemisorption Analyzer). X-ray photoelectron spectroscopy (XPS, AXIS SUPRA) data were acquired using Mg-K$\alpha$ radiation (1253.6 eV); the spectra were fitted using the Shirley background and the Gaussian–Lorentzian lineshape analysis.

## Methane combustion measurement

The activity for methane oxidation was measured in a fixed-bed flow reactor consisting of a 10 mm-diameter quartz glass tube. The mixed gas comprised 0.2 vol% CH$_4$ in air at a total flow rate of 60 mL min$^{-1}$ (mass hourly space velocity = 12 000 L kg$^{-1}$ h$^{-1}$)

and was passed over 0.3 g of the catalyst; the gas was supplied to the catalyst bed using a mass flow controller. Prior to the measurements, the catalysts were pretreated at 400 °C for 2 h under a flow of argon (100 mL min$^{-1}$). The concentration of methane gas at the outlet was analyzed using a non-dispersive infrared (NDIR) gas analyzer (DA-770, GASDNA Co., Ltd). The reaction temperature was increased from 150 to 500 °C in 25 °C intervals, and the methane conversion at each point was obtained after stabilization for 15 min.

## Results and discussion

### Crystal structure of Sr–Fe perovskite-based catalysts

The crystal structure of the $Sr_3Fe_2O_7$ powders was determined through X-ray diffraction (XRD) analysis using Rietveld refinement. The detailed crystallographic data and structure refinement parameters obtained by Rietveld refinement analysis are summarized in Tables 1 and S2.† The analysis used crystal structure data obtained from the inorganic crystal structure database ($Sr_3Fe_2O_7$: ICSD #74422) as a reference. Fig. 1(a) and (b) displays the XRD patterns and crystal structure of the $Sr_3Fe_2O_7$ powders synthesized in this study.

The XRD data matched well with the lattice constants of $Sr_3Fe_2O_7$ (ICSD #74422), albeit with some $SrFeO_{2.75}$ as an impurity phase. Rietveld refinement yielded favorable weighted profile R-factors, confirming the phase purity of the samples. At room temperature, $Sr_3Fe_2O_7$ was found to crystallize in a tetragonal system (space group $I_4/mmm$) with lattice parameters $a = 3.86239$ nm, $b = 3.86239$ nm, and $c = 20.15442$ nm (see Table 1). The mass fraction of $Sr_3Fe_2O_7$ in the synthesized powder was determined to be 96%, making it the predominant phase. The $Sr_3Fe_2O_7$ oxide exhibited the RP-type structure composed of $(SrFeO_3)_2(SrO)$. A second perovskite-type phase, $SrFeO_{2.75}$, was also present. As a promoter, the synthesized $Sr_3Fe_2O_7$ was used to create a composite oxide catalyst for low-temperature methane combustion. For this purpose, a composite oxide catalyst, composed of 10wt%PdO/16wt%$Sr_3Fe_2O_{7-\delta}/\alpha-Al_2O_3$, was synthesized by varying the composition. The composition of the samples was analyzed by ICP-OES
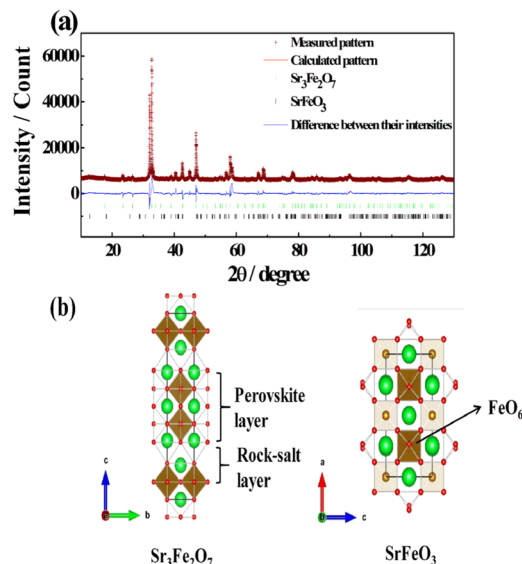


**Fig. 1** (a) Rietveld refinement of X-ray powder diffraction data for $Sr_3Fe_2O_7$; white symbol: measured pattern, red solid line: calculated pattern, blue solid line: difference between the intensities and (b) crystal structure of $Sr_3Fe_2O_7$ and $SrFeO_{2.75}$. The circles correspond to Sr cations (green) and oxygen anions (red), which are located at the corners of an $FeO_6$ octahedron.

and the results are summarized in Table S3.† It was confirmed that all samples were synthesized in each stoichiometric ratio. XRD patterns of the synthesized catalysts were compared with those of 10wt%PdO/$Sr_3Fe_2O_{7-\delta}$, 10wt%PdO/$\alpha-Al_2O_3$, and 16wt% $Sr_3Fe_2O_{7-\delta}/\alpha-Al_2O_3$ as shown in Fig. 2. The XRD pattern of the 10wt%PdO/$Sr_3Fe_2O_{7-\delta}$ catalyst showed PdO and the ortho-rhombic $SrFeO_{2.75}$ ($SrFeO_{3-\delta}$) perovskite phase. Supporting PdO on $Sr_3Fe_2O_7$ led to the transformation of the RP-type $Sr_3Fe_2O_7$ structure into the simple perovskite-type $SrFeO_{3-\delta}$, likely due to the migration of oxide ions from $Sr_3Fe_2O_7$ to the Pd active sites.

In contrast, the XRD pattern of the 10wt%PdO/16wt%$Sr_3Fe_2O_{7-\delta}/\alpha-Al_2O_3$ catalyst showed PdO, tetragonal $Sr_3Fe_2O_7$

**Table 1** Crystallographic data and refined lattice parameters of $Sr_3Fe_2O_7$ (main phase) and $SrFeO_{2.75}$ (second phase) obtained via Rietveld refinement using the X-ray powder diffraction data acquired at room temperature

|  | $Sr_3Fe_2O_7$ | $SrFeO_{2.75}$ |
|---|---|---|
| Crystal system | Tetragonal | Orthorhombic |
| Space group | $I_4/mmm$ | $Cmmm$ |
| $a$ (nm) | 3.86239 | 9.75109 |
| $b$ (nm) | 3.86239 | 9.81500 |
| $c$ (nm) | 20.15442 | 2.91472 |
| Mass fractions of the phases | 0.9603 | 0.0397 |
| $R_{wp}$ (%) | 6.379 | |
| $R_p$ (%) | 3.343 | |
| $S$ (%) | 5.2009 | |
| $d_1$ | 0.0867 | |
| $d_2$ | 0.0531 | |
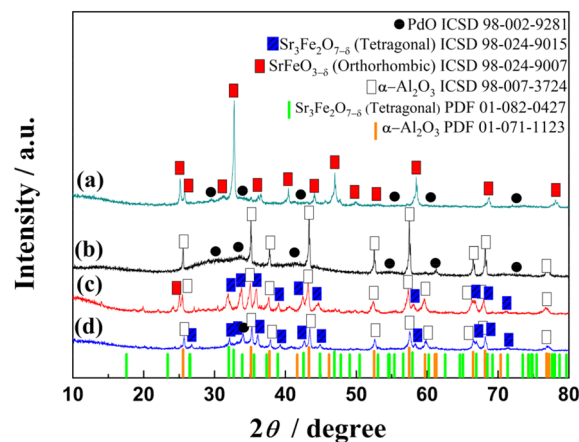


**Fig. 2** XRD pattern of (a) 10wt%PdO/$SrFeO_{3-\delta}$, (b) 10wt%PdO/$\alpha-Al_2O_3$, (c) 16wt%$Sr_3Fe_2O_{7-\delta}/\alpha-Al_2O_3$, and (d) 10wt%PdO/16wt%$Sr_3Fe_2O_{7-\delta}/\alpha-Al_2O_3$ catalysts.

($Sr_3Fe_2O_{7-\delta}$) perovskite phase with space group $I_4/mmm$, $\alpha$-$Al_2O_3$ and $\gamma$-$Al_2O_3$ phase, in which phase ratio of the $\alpha$-$Al_2O_3$ and $\gamma$-$Al_2O_3$ phase was 84.4 : 15.6% form the Rietveld refinement. In the XRD patterns of the 16wt%$Sr_3Fe_2O_{7-\delta}$/$\alpha$-$Al_2O_3$ catalyst, a small amount of $\gamma$-$Al_2O_3$ phase was also obtained and the phase ratio of $\gamma$-$Al_2O_3$ phase was 17.3%. This confirmed the preservation of the $Sr_3Fe_2O_7$ perovskite phase when supported on $\alpha$-$Al_2O_3$, indicating improved structural stability. In addition, $\alpha$-$Al_2O_3$ contributes to the enhancement of the dispersity of the PdO on catalyst promoter. The crystallite size of the PdO of 10wt%PdO/$SrFeO_{3-\delta}$, 10wt%PdO/16wt% $Sr_3Fe_2O_{7-\delta}$/$\alpha$-$Al_2O_3$, and 10wt%PdO/$\alpha$-$Al_2O_3$ was calculated using Scherrer's equation. As shown in Table 2, the structural effects were supported by differences in PdO crystallite sizes, with the 10wt%PdO/$SrFeO_{3-\delta}$ catalyst exhibiting larger crystallites compared to the 10wt%PdO/16wt%$Sr_3Fe_2O_{7-\delta}$/$\alpha$-$Al_2O_3$. This difference indicates that the bulk migration of the oxide ions from $Sr_3Fe_2O_7$ to the Pd active site in the 10wt%PdO/$SrFeO_{3-\delta}$ catalyst without the $\alpha$-$Al_2O_3$ support can facilitate oxidation and aggregation of the Pd active centers, which increases the size of the PdO crystallites. In addition, this result was also supported by the PdO dispersion on the respective catalysts. The PdO dispersion of 10wt%PdO/16wt%$Sr_3Fe_2O_{7-\delta}$/$\alpha$-$Al_2O_3$ (7.69%) was determined to be higher than that of 10wt%PdO/$SrFeO_{3-\delta}$ (7.58%), as shown in Table S4.† In comparison, the 10wt%PdO/$\alpha$-$Al_2O_3$ catalyst without the $Sr_3Fe_2O_7$ promoter had the smallest PdO crystallite size (3.71 nm) because there was no source of oxide ions for migration to the PdO active species.

To determine an amount of PdO on the surface of the catalysts, we carried out XPS analysis for 10wt%PdO/$SrFeO_{3-\delta}$ and 10wt%PdO/16wt%$Sr_3Fe_2O_{7-\delta}$/$\alpha$-$Al_2O_3$, and calculated the $Pd^{2+}$/($Pd^{2+}$ + $Pd^0$) ratio using peak areas of Pd 3d core-level (see in Fig. S3 and Table S4†). The Pd 3d XPS spectra comprise two spin–orbit multiplets corresponding to the $3d_{3/2}$ and $3d_{5/2}$ core levels, and each peak of the $3d_{3/2}$ and $3d_{5/2}$ core levels can be divided into two Gaussian peaks, where peak at high binding energy corresponds to the $Pd^{2+}$ and the other peak at low binding energy corresponds to the $Pd^0$. The $Pd^{2+}$/($Pd^{2+}$ + $Pd^0$) ratio of 10wt%PdO/$SrFeO_{3-\delta}$ (42.49%) was higher than that of 10wt%PdO/16wt%$Sr_3Fe_2O_{7-\delta}$/$\alpha$-$Al_2O_3$ (40.31%). This result indicates that a larger amount of PdO was loaded onto the surface of 10wt%PdO/$SrFeO_{3-\delta}$ compared to the 10wt%PdO/

16wt%$Sr_3Fe_2O_{7-\delta}$/$\alpha$-$Al_2O_3$ and it also supports that bulk migration of the oxide ions from the promoter to the Pd active sites was more extensively occurred at the sample of 10wt%PdO/$SrFeO_{3-\delta}$. In addition, the 10wt%PdO/16wt%$Sr_3Fe_2O_{7-\delta}$/$\alpha$-$Al_2O_3$ catalyst (70.19 $m^2$ $g^{-1}$) exhibited a higher specific surface area than that of 10wt%PdO/$SrFeO_{3-\delta}$ catalyst (21.58 $m^2$ $g^{-1}$) without supporting $Al_2O_3$ as shown in Table 2. On the other hand, the specific surface area of 10wt%PdO/$\alpha$-$Al_2O_3$ catalyst (2.51 $m^2$ $g^{-1}$) was lower than that of 10wt%PdO/$SrFeO_{3-\delta}$ catalyst. This result indicates that a high specific surface area of the 10wt%PdO/16wt%$Sr_3Fe_2O_{7-\delta}$/$\alpha$-$Al_2O_3$ catalyst may be due to the presence of the $\gamma$-$Al_2O_3$ phase, which usually contributes to the enhancement of the specific surface area of catalyst materials.

To investigate the effect of the $\alpha$-$Al_2O_3$ support on the thermal and structural stability of the catalysts, the 10wt%PdO/16wt%$Sr_3Fe_2O_{7-\delta}$/$\alpha$-$Al_2O_3$ and 10wt%PdO/$SrFeO_{3-\delta}$ catalysts were evaluated at various temperatures, 200–600 °C. The catalyst samples were re-heated at each temperature for 1 h and their crystal structure was identified (see in Fig. S1†). In the case of the 10wt%PdO/16wt%$Sr_3Fe_2O_{7-\delta}$/$\alpha$-$Al_2O_3$, the $Sr_3Fe_2O_{7-\delta}$ perovskite structure was well maintained in all samples re-heated at 200–600 °C. On the other hand, the $SrFeO_{3-\delta}$ perovskite structure for 10wt%PdO/$SrFeO_{3-\delta}$ was transformed to a composite phase of $SrFe_{12}O_{19}$ and $Sr_2Fe_2O_5$ after heat treatment at 200 °C. It indicates that $\alpha$-$Al_2O_3$ is significantly effective in inhibiting the crystal structure change for these catalysts. Moreover, when $Sr_3Fe_2O_7$ was supported on $\alpha$-$Al_2O_3$, the XRD peak of the $Sr_3Fe_2O_7$ perovskite phase shifted to the lower angle side (refer to Fig. S7†), which indicates that the lattice of the $Sr_3Fe_2O_7$ perovskite structure was expanded by the formation of oxygen vacancies in the $Sr_3Fe_2O_7$ lattice. The release of oxide ions from $Sr_3Fe_2O_7$ can be associated with transformation of the $\gamma$-$Al_2O_3$ monoclinic phase, the raw material used for the support, into the hexagonal $\alpha$-$Al_2O_3$ phase with a volume reduction of $\sim$10% after calcination at 1000 °C during synthesis of the catalyst.[50] This result confirms that in the case of the 16wt% $Sr_3Fe_2O_{7-\delta}$/$\alpha$-$Al_2O_3$ and 10wt%PdO/16wt%$Sr_3Fe_2O_{7-\delta}$/$\alpha$-$Al_2O_3$ catalysts, the $Sr_3Fe_2O_{7-\delta}$ promoter with oxygen vacancies was formed without any change in the RP-type $Sr_3Fe_2O_7$ perovskite structure when $Sr_3Fe_2O_7$ was supported on $\alpha$-$Al_2O_3$.

## Surface and bulk oxide property of Sr–Fe perovskite-based catalysts

To investigate the surface acidic and basic property of the prepared Sr–Fe perovskite-based catalysts, $NH_3$- and $CO_2$-TPD measurements were evaluated as shown in Fig. 3(a) and (b). The 10wt%PdO/16wt%$Sr_3Fe_2O_{7-\delta}$/$\alpha$-$Al_2O_3$ catalyst displayed narrow desorption peaks at around 100, 230, and 490 °C in the $NH_3$-TPD profile, signifying weak, medium-strength, and strongly acidic sites, including Lewis acid sites. In comparison, the 10wt%PdO/$SrFeO_{3-\delta}$, 10wt%PdO/$\alpha$-$Al_2O_3$, and $\alpha$-$Al_2O_3$ catalysts exhibited broad and narrow peaks mainly associated with weak acid sites and Lewis acid sites. In the $CO_2$-TPD profiles, the 10wt%PdO/16wt%$Sr_3Fe_2O_{7-\delta}$/$\alpha$-$Al_2O_3$ catalyst showed a pronounced area peak at around 110 °C, while the other

**Table 2** PdO crystallite size and specific surface area of $\gamma$-$Al_2O_3$, $\alpha$-$Al_2O_3$, $Sr_3Fe_2O_7$, 10wt%PdO/$SrFeO_{3-\delta}$, 10wt%PdO/$\alpha$-$Al_2O_3$, 16wt% $Sr_3Fe_2O_{7-\delta}$/$\alpha$-$Al_2O_3$, and 10wt%PdO/16wt%$Sr_3Fe_2O_{7-\delta}$/$\alpha$-$Al_2O_3$ catalysts

| Sample | PdO crystallite size/nm | Specific surface area/$m^2$ $g^{-1}$ |
|---|---|---|
| $\gamma$-$Al_2O_3$ | — | 148.0 |
| $\alpha$-$Al_2O_3$ | — | 14.6 |
| $Sr_3Fe_2O_7$ | — | 30.5 |
| 10wt%PdO/$SrFeO_{3-\delta}$ | 19.1 | 21.6 |
| 10wt%PdO/$\alpha$-$Al_2O_3$ | 3.7 | 2.5 |
| 16wt%$Sr_3Fe_2O_{7-\delta}$/$\alpha$-$Al_2O_3$ | — | 80.9 |
| 10wt%PdO/16wt%$Sr_3Fe_2O_{7-\delta}$/$\alpha$-$Al_2O_3$ | 9.2 | 70.2 |

**Fig. 3** (a) $NH_3$-TPD and (b) $CO_2$-TPD profiles of $\alpha$-$Al_2O_3$, 10wt%PdO/$\alpha$-$Al_2O_3$, 10wt%PdO/$SrFeO_{3-\delta}$, and 10wt%PdO/16wt%$Sr_3Fe_2O_{7-\delta}$/$\alpha$-$Al_2O_3$. (c) $H_2$-TPR profile of $\alpha$-$Al_2O_3$, $Sr_3Fe_2O_7$, 16wt%$Sr_3Fe_2O_{7-\delta}$/$\alpha$-$Al_2O_3$, 10wt%PdO/$\alpha$-$Al_2O_3$, 10wt%PdO/$SrFeO_{3-\delta}$, and 10wt%$Sr_3Fe_2O_{7-\delta}$/$\alpha$-$Al_2O_3$. (d) $O_2$-TPD profile of $Sr_3Fe_2O_7$, 16wt%$Sr_3Fe_2O_{7-\delta}$/$\alpha$-$Al_2O_3$, 10wt%PdO/$SrFeO_{3-\delta}$, and 10wt%PdO/16wt%$Sr_3Fe_2O_{7-\delta}$/$\alpha$-$Al_2O_3$.

catalysts showed weak $CO_2$ adsorption. This result indicates that the 10wt%PdO/16wt% $Sr_3Fe_2O_{7-\delta}$/$\alpha$-$Al_2O_3$ has the superior basic sites compared to that of the other catalysts. The number of acidic and basic sites on each catalyst was determined from peak areas in the $NH_3$- and $CO_2$-TPD profiles. As shown in Table 3, the number of acidic sites on the catalyst was dramatically increased when PdO was supported on $\alpha$-$Al_2O_3$, which is due to the increased acidic sites of $Pd^{2+}$ cations on the catalyst surface. The highest number of basic sites was obtained for the 10wt% PdO/16wt%$Sr_3Fe_2O_{7-\delta}$/$\alpha$-$Al_2O_3$ catalyst (220.0 $\mu$mol $g^{-1}$), which is higher than that of 10wt%PdO/$SrFeO_{3-\delta}$ (148 $\mu$mol $g^{-1}$). This

result indicates that the concentration of surface oxygen species which act as a Lewis basic site on the 16wt%$Sr_3Fe_2O_{7-\delta}$/$\alpha$-$Al_2O_3$ is higher than that on the $SrFeO_{3-\delta}$ bulk, which may be due to the surface area of 16wt%$Sr_3Fe_2O_{7-\delta}$/$\alpha$-$Al_2O_3$ was higher than that of $SrFeO_{3-\delta}$ bulk.

To investigate the oxygen migration properties of the prepared Sr–Fe perovskite-based catalysts, $H_2$-TPR and $O_2$ pulse injection measurements were performed (Fig. 3(c), S2† and Table 3). The $\alpha$-$Al_2O_3$ support showed no $H_2$ reduction activity or oxygen storage capacity. The $H_2$-TPR profile of the $Sr_3Fe_2O_7$ perovskite bulk oxide exhibited $H_2$ reduction peaks at high

**Table 3** Number of acidic, basic sites, reduction peak temperature, $H_2$ consumption amount and oxygen storage capacity (OSC), amount of oxygen desorption site, and surface oxygen vacancy density for $\alpha$-$Al_2O_3$, $Sr_3Fe_2O_7$, 16wt%$Sr_3Fe_2O_{7-\delta}$/$\alpha$-$Al_2O_3$, 10wt%PdO/$\alpha$-$Al_2O_3$, 10wt%PdO/$SrFeO_{3-\delta}$, and 10wt%PdO/16wt%$Sr_3Fe_2O_{7-\delta}$/$\alpha$-$Al_2O_3$

| Sample | Number of acidic site/$\mu$mol $g^{-1}$ | Number of basic site/$\mu$mol $g^{-1}$ | Reduction temperature/°C | $H_2$ consumption amount/mmol $g^{-1}$ | OSC/$\mu$mol $O_2 \cdot g^{-1}$ | $O_2$ desorption site/$\mu$mol $g^{-1}$ | Oxygen vacancy density/$\times 10^{17}$ sites $m^{-2}$ |
|---|---|---|---|---|---|---|---|
| $\alpha$-$Al_2O_3$ | 27.5 | 53.8 | — | 0 | 0 | — | — |
| $Sr_3Fe_2O_7$ | — | — | 450, 495 | 1.237($SrFeO_x$) | 4.899 | 44 | 1.59 |
| 16wt%$Sr_3Fe_2O_{7-\delta}$/$\alpha$-$Al_2O_3$ | — | — | 345 | 0.111($SrFeO_x$) | 1.752 | 84 | 3.95 |
| 10wt%PdO/$\alpha$-$Al_2O_3$ | 41.0 | 15.5 | 62 | 0.258(PdO) | 0.703 | — | — |
| 10wt%PdO/$SrFeO_{3-\delta}$ | 109.5 | 148.2 | 73, 325, 440, 495 | 0.587(PdO) 2.119($SrFeO_x$) | 35.174 | 75 | 3.21 |
| 10wt%PdO/16wt% $Sr_3Fe_2O_{7-\delta}$/$\alpha$-$Al_2O_3$ | 169.0 | 220.0 | 56, 83, 193, 420, 490 | 0.104(PdO) 0.677($SrFeO_x$) | 35.695 | 357 | 15.44 |

temperatures of around 450 and 495 °C by bulk oxygen species. In contrast, the $16wt\%Sr_3Fe_2O_{7-\delta}/\alpha-Al_2O_3$ showed a lower temperature $H_2$ reduction peak at 345 °C by surface oxygen reduction. It is because that the higher specific surface area and the more surface oxygen species, the lower the activation energy required for oxygen release induced to facilitate $H_2$ reduction even at low temperatures. The $16wt\%Sr_3Fe_2O_{7-\delta}/\alpha-Al_2O_3$ catalyst exhibited lower $H_2$ consumption amount and oxygen storage capacity (OSC) than the $Sr_3Fe_2O_7$ perovskite bulk due to the small absolute amount of oxygen species released from the lattice of $Sr_3Fe_2O_{7-\delta}$. When assessing supported PdO species, the PdO reduction peak of $10wt\%PdO/16wt\%Sr_3Fe_2O_{7-\delta}/\alpha-Al_2O_3$ catalyst was exhibited at the lowest temperature of 56 °C compared to $10wt\%PdO/\alpha-Al_2O_3$ (62 °C) and $10wt\%PdO/SrFeO_{3-\delta}$ (73 °C). The $H_2$ consumption amount of PdO reduction peak were determined as follows; $10wt\%PdO/SrFeO_{3-\delta}$ (587 $\mu mol\ g^{-1}$) > $10wt\%PdO/\alpha-Al_2O_3$ (258 $\mu mol\ g^{-1}$) > $10wt\%PdO/16wt\%Sr_3Fe_2O_{7-\delta}/\alpha-Al_2O_3$ (104 $\mu mol\ g^{-1}$). The reduction peak of $SrFeO_x$ oxide in the $10wt\%PdO/16wt\%Sr_3Fe_2O_{7-\delta}/\alpha-Al_2O_3$ catalyst occurred at lower temperatures (83, 193, 420 and 490 °C) than that in the $10wt\%PdO/SrFeO_{3-\delta}$ catalyst (325, 440 and 495 °C). The $H_2$ consumption amount of $SrFeO_x$ oxide reduction peak were determined as follows; $10wt\%PdO/SrFeO_{3-\delta}$ (2119 $\mu mol\ g^{-1}$) > $10wt\%PdO/16wt\%Sr_3Fe_2O_{7-\delta}/\alpha-Al_2O_3$ (677 $\mu mol\ g^{-1}$). As the PdO active species was supported, the activation energy for oxygen release from $SrFeO_x$ oxide was reduced, and then, $H_2$ consumption amount and OSC of PdO supported catalysts tended to increase compared to catalyst without PdO supported. On the other hand, although $H_2$ consumption amount was low, the $10wt\%PdO/16wt\%Sr_3Fe_2O_{7-\delta}/\alpha-Al_2O_3$ catalyst, which has high concentration of surface oxygen species, showed more low-temperature activity for $H_2$ reduction than the $10wt\%PdO/SrFeO_{3-\delta}$ catalyst, which has mainly bulk oxygen species. $O_2$-TPD analysis was performed to confirm the formation of oxygen vacancies on the surface of prepared catalysts and the results are shown in Fig. 3(d) and Table 3. The $16wt\%Sr_3Fe_2O_{7-\delta}/\alpha-Al_2O_3$ showed a higher $O_2$ desorption area than that of the $Sr_3Fe_2O_7$ perovskite bulk oxide at low temperature of around 100 °C. The $O_2$ desorption at low temperature can be induced from physically adsorbed oxygen on surface oxygen vacancy. The $16wt\%Sr_3Fe_2O_{7-\delta}/\alpha-Al_2O_3$ showed a higher oxygen vacancy density which estimated based on the amount of ad-$O_2$ derived from the $O_2$-TPD than that of the $Sr_3Fe_2O_7$ bulk (Table 3). This result indicates that the surface oxygen vacancy of the $16wt\%Sr_3Fe_2O_{7-\delta}/\alpha-Al_2O_3$ is a higher than that of the $Sr_3Fe_2O_7$ perovskite. This is because that the lattice of the $Sr_3Fe_2O_7$ perovskite structure of $16wt\%Sr_3Fe_2O_{7-\delta}/\alpha-Al_2O_3$ was expanded by the formation of oxygen vacancies as the oxygen ions are released from $Sr_3Fe_2O_7$ lattice associated with the transformation of the $\gamma-Al_2O_3$ monoclinic phase into the $\alpha-Al_2O_3$ hexagonal phase. The $O_2$ desorption area of the catalysts was effectively increased when PdO was supported on the surface of the catalysts. and the $O_2$ desorption area. and the oxygen vacancy density of $10wt\%PdO/16wt\%Sr_3Fe_2O_{7-\delta}/\alpha-Al_2O_3$ was superior to $10wt\%PdO/SrFeO_{3-\delta}$. These results indicate that the amount of oxygen ions released from the surface oxygen and migrating to the Pd active sites is higher for 16wt%

$Sr_3Fe_2O_{7-\delta}/\alpha-Al_2O_3$ due to the high oxygen ion conductivity and the oxygen vacancy density compared to the $Sr_3Fe_2O_7$ bulk. This usually results in the high methane gas decomposition performance of catalysts.

## Catalytic activity for methane combustion over Sr–Fe perovskite-based catalyst

The catalytic activity of catalysts with different compositions for methane combustion was evaluated. Fig. 4 illustrates the temperature dependence of methane combustion over the various prepared catalysts, including $10wt\%PdO/SrFeO_{3-\delta}$, $10wt\%PdO/\alpha-Al_2O_3$, $16wt\%Sr_3Fe_2O_{7-\delta}/\alpha-Al_2O_3$, and $10wt\%PdO/16wt\%Sr_3Fe_2O_{7-\delta}/\alpha-Al_2O_3$.

The $10wt\%PdO/\alpha-Al_2O_3$ catalyst enabled complete methane combustion at 400 °C. Upon the addition of the $Sr_3Fe_2O_{7-\delta}$ co-catalyst to the $10wt\%PdO/\alpha-Al_2O_3$ catalyst, the temperature for complete methane combustion decreased to 325 °C. This result indicates that catalytic activity for methane combustion at low temperatures can be enhanced by adding the $Sr_3Fe_2O_{7-\delta}$ co-catalyst, which increase surface oxygen species and oxygen vacancy density of the catalyst, thus promoting methane oxidation at low-temperature. To confirm the promoting effect of the PdO active sites and $\alpha-Al_2O_3$ support on catalytic methane combustion, we compared the catalytic activity of the $16wt\%Sr_3Fe_2O_{7-\delta}/\alpha-Al_2O_3$ and $10wt\%PdO/SrFeO_{3-\delta}$ catalysts with that of the $10wt\%PdO/16wt\%Sr_3Fe_2O_{7-\delta}/\alpha-Al_2O_3$ catalyst. The $16wt\%Sr_3Fe_2O_{7-\delta}/\alpha-Al_2O_3$ showed limited catalytic activity for methane combustion. Since methane oxidation primarily occurs on the PdO active sites, the $10wt\%PdO/SrFeO_{3-\delta}$ catalysts achieved complete methane combustion at 425 °C, approximately 100 °C higher than the $10wt\%PdO/16wt\%Sr_3Fe_2O_{7-\delta}/\alpha-Al_2O_3$ catalyst. This difference arises from the fact that the $10wt\%PdO/SrFeO_{3-\delta}$ catalysts exhibit lower surface oxygen species and oxygen vacancy density compared to the $10wt\%PdO/16wt\%Sr_3Fe_2O_{7-\delta}/\alpha-Al_2O_3$ catalysts, attributed to the high activation energy for oxygen migration in $SrFeO_{3-\delta}$ compared to the $Sr_3Fe_2O_{7-\delta}$ perovskite oxide. Among the



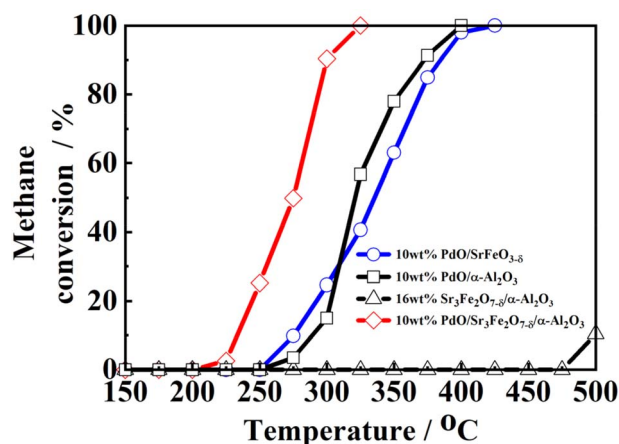**Fig. 4** Temperature-dependence of methane oxidation over $10wt\%PdO/SrFeO_{3-\delta}$, $10wt\%PdO/\alpha-Al_2O_3$, $16wt\%Sr_3Fe_2O_{7-\delta}/\alpha-Al_2O_3$, and $10wt\%PdO/16wt\%Sr_3Fe_2O_{7-\delta}/\alpha-Al_2O_3$ catalysts.

prepared catalysts with different compositions, the highest catalytic activity was achieved with the 10wt%PdO/16wt%Sr$_3$Fe$_2$O$_{7-\delta}$/$\alpha$-Al$_2$O$_3$ catalyst sample, where a methane conversion of 100% was attained at 325 °C. Nevertheless, when compared to cerium oxide (CeO$_2$)-based catalysts with higher oxygen storage capacity than Sr$_3$Fe$_2$O$_{7-\delta}$ perovskite oxide,[51–55,57] the catalytic methane combustion activity of the 10wt%PdO/16wt% Ce$_{0.92}$Si$_{0.08}$O$_{2-\delta}$/$\gamma$-Al$_2$O$_3$ catalysts[56] was still higher than that of the 10wt% PdO/16wt%Sr$_3$Fe$_2$O$_{7-\delta}$/$\alpha$-Al$_2$O$_3$ catalysts under low temperature below 300 °C as shown in Fig. S6.†

For a more detailed investigation of the methane decomposition mechanism of the Sr$_3$Fe$_2$O$_{7-\delta}$ perovskite oxide-based catalyst, XPS analysis of Fe 2p and O 1s before and after the reaction was performed,[58–60] as presented in Fig. S4, S5, and Table S4.† An increase in the ratio of Fe$^{3+}$/Fe and a decrease in the ratio of Fe$^{4+}$/Fe can be observed in both SrFeO$_{3-\delta}$ and Sr$_3$Fe$_2$O$_{7-\delta}$ before and after methane combustion reaction. This implies that the reduction of FeO$_2$ to Fe$_2$O$_3$ occurs during the methane decomposition reaction, activating the redox property of the catalyst due to the valence change of Fe$^{3+/4+}$. In result of O 1s analysis, the ratio of surface oxygen species (O$_{ads}$/O) (53.67%) was higher than the ratio of lattice oxygen species (O$_{latt}$/O) (46.67%) in before reaction of 10wt%PdO/16wt%Sr$_3$Fe$_2$O$_{7-\delta}$/$\alpha$-Al$_2$O$_3$. On the other hand, the ratio of surface oxygen species (O$_{ads}$/O) (33.25%) was lower than the ratio of lattice oxygen species (O$_{latt}$/O) (66.75%) in before reaction of 10wt%PdO/SrFeO$_{3-\delta}$. And then, no the fraction of surface oxygen species was measured in XPS spectra of O 1s of 10wt%PdO/$\alpha$-Al$_2$O$_3$. From this result, it can be confirmed that the highest concentration of surface oxygen species is distributed on 10wt%PdO/16wt%Sr$_3$Fe$_2$O$_{7-\delta}$/$\alpha$-Al$_2$O$_3$ compared to 10wt%PdO/SrFeO$_{3-\delta}$ and 10wt%PdO/$\alpha$-Al$_2$O$_3$. Additionally, a relative decrease in the ratio of surface oxygen species (O$_{ads}$/O) can be observed before and after the reaction with increase of the ratio of lattice oxygen species (O$_{latt}$/O) in SrFeO$_x$ promoted catalysts. This indicates that the surface oxygen species of the catalyst actively participate in the reaction activity during the methane combustion reaction. Moreover, the high Fe$^{3+}$/Fe and O$_{ads}$/O ratios after the reaction indicate that the mobility of surface oxygen associated with the reduction of FeO$_2$ to Fe$_2$O$_3$ was higher for 10wt%PdO/16wt%Sr$_3$Fe$_2$O$_{7-\delta}$/$\alpha$-Al$_2$O$_3$ than for 10wt%PdO/SrFeO$_{3-\delta}$.

For a more detailed discussion of the effects of catalyst composition on the catalytic activity for low-temperature methane combustion, we calculated the turnover frequency (TOF) to density of surface PdO active site, oxygen vacancies and specific reaction rates for methane conversion at 275 °C. Table 4 presents the methane conversion, specific reaction rate ($r_{275°C}$) and TOF at 275 °C to the density of PdO active site (PdO) and

oxygen vacancies for the 10wt%PdO/$\alpha$-Al$_2$O$_3$, 10wt%PdO/SrFeO$_{3-\delta}$, and 10wt%PdO/16wt%Sr$_3$Fe$_2$O$_{7-\delta}$/$\alpha$-Al$_2$O$_3$ catalysts. The 10wt%PdO/16wt%Sr$_3$Fe$_2$O$_{7-\delta}$/$\alpha$-Al$_2$O$_3$ catalyst exhibited the highest reaction rate (0.619 mmol s$^{-1}$ g$^{-1}$) compared to that of the 10wt%PdO/SrFeO$_{3-\delta}$ (0.132 mmol s$^{-1}$ g$^{-1}$) and 10wt%PdO/$\alpha$-Al$_2$O$_3$ (0.75 mmol s$^{-1}$ g$^{-1}$) catalysts, which is consistent with the catalytic methane conversion activities as shown in Fig. 4. In particular, the TOF derived from normalization of the rate constant with the surface density of PdO active sites was found to increase as the SrFeO$_x$ oxide supported to 10wt%PdO/$\alpha$-Al$_2$O$_3$, reaching 7.955 × 10$^3$ h$^{-1}$ for the 10wt%PdO/16wt%Sr$_3$Fe$_2$O$_{7-\delta}$/$\alpha$-Al$_2$O$_3$. When methane is decomposition at the PdO active site, even under the same PdO loading conditions, the TOF value increases as the SrFeO$_x$ oxide is loaded. This is because the oxygen species released by SrFeO$_x$ increases the oxidizing properties of the PdO active species. Moreover, the TOF derived from normalization of the rate constant with the surface density of oxygen vacancy in the 10wt%PdO/16wt%Sr$_3$Fe$_2$O$_{7-\delta}$/$\alpha$-Al$_2$O$_3$ was superior to 10wt%PdO/SrFeO$_{3-\delta}$, reaching 36.10 × 10$^3$ h$^{-1}$ for the most activity, which is consistent with the catalytic methane conversion activities. This observation confirms that by supporting the Sr$_3$Fe$_2$O$_{7-\delta}$ co-catalyst, the catalytic activity for low-temperature methane combustion can be facilitated by improving the density of oxygen vacancy. Therefore, it can be concluded that, despite having identical PdO loadings, these factors are the primary contributors to the superior methane oxidation capacity of the PdO active species in 10wt%PdO/16wt% Sr$_3$Fe$_2$O$_{7-\delta}$/$\alpha$-Al$_2$O$_3$ compared to those in the 10wt%PdO/SrFeO$_{3-\delta}$ catalysts.

### Effect of PdO loading in Sr–Fe perovskite-based catalyst

To investigate the impact of PdO loading on the catalytic activity for methane combustion, we synthesized a series of $\alpha$wt%PdO/16wt%Sr$_3$Fe$_2$O$_{7-\delta}$/$\alpha$-Al$_2$O$_3$ catalysts (1 ≤ $\alpha$ ≤ 20) and evaluated their catalytic performance. The X-ray diffraction (XRD) peaks in Fig. 5(a) were accurately indexed to PdO, the Sr$_3$Fe$_2$O$_6$ phase, and $\alpha$-Al$_2$O$_3$, with no impurity phases detected. Notably, the intensity of the PdO peak increased with higher PdO loading, leading to an increased calculated crystallite size of PdO (refer to Table 5). Conversely, the specific surface area of the $\alpha$wt%PdO/16wt%Sr$_3$Fe$_2$O$_{7-\delta}$/$\alpha$-Al$_2$O$_3$ catalysts (1 ≤ $\alpha$ ≤ 20) decreased as PdO loading increased (see Table 5). This decrease can be attributed to the aggregation of PdO particles on the catalyst's surface. High-resolution TEM images obtained via Cs-TEM revealed Pd(200) crystal lattices with a $d$-spacing of 0.22 nm in 13wt%PdO/16wt%Sr$_3$Fe$_2$O$_{7-\delta}$/$\alpha$-Al$_2$O$_3$ catalysts (see Fig. S8(b)†). The particle size of PdO was approximately 6–7 nm, which is

**Table 4** Methane conversion, specific reaction rate ($r_{275 °C}$) and turnover frequency (TOF) at 275 °C the density of PdO active site (PdO) and oxygen vacancies over the 10wt%PdO/$\alpha$-Al2O$_3$, 10wt%PdO/SrFeO$_{3-\delta}$, and 10wt%PdO/16wt% Sr$_3$Fe$_2$O$_{7-\delta}$/$\alpha$-Al$_2$O$_3$

| Sample | Methane conversion at 275 °C/% | $r_{275°C}$/mmol$^{-1}$ g$^{-1}$ | TOF × 10$^3$/h$^{-1}$ (PdO) | TOF × 10$^3$/h$^{-1}$ (oxygen vacancies) |
|---|---|---|---|---|
| 10wt%PdO/$\alpha$-Al$_2$O$_3$ | 3.50 | 0.075 | 0.002 | — |
| 10wt%PdO/SrFeO$_{3-\delta}$ | 9.85 | 0.132 | 0.103 | 7.28 |
| 10wt%PdO/16wt% Sr$_3$Fe$_2$O$_{7-\delta}$/$\alpha$-Al$_2$O$_3$ | 49.85 | 0.619 | 7.955 | 36.10 |
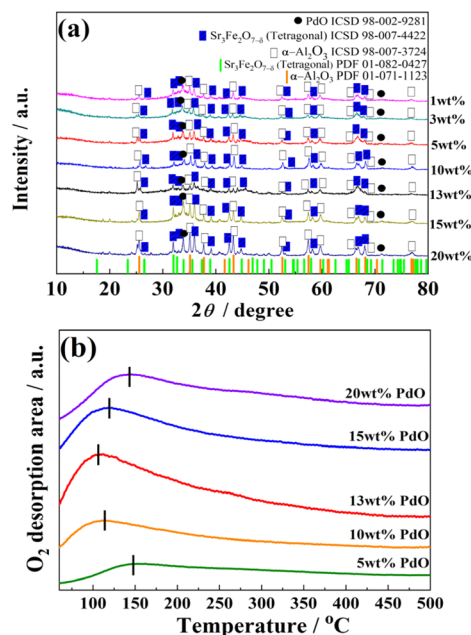
**Fig. 5** (a) XRD pattern of $\alpha$wt%PdO/16wt%Sr$_3$Fe$_2$O$_{7-\delta}$/$\alpha$-Al$_2$O$_3$ catalysts with different PdO loadings ($\alpha = 1, 3, 5, 10, 13, 15, 20$). (b) O$_2$-TPD profile of $\alpha$wt%PdO/16wt%Sr$_3$Fe$_2$O$_{7-\delta}$/$\alpha$-Al$_2$O$_3$ catalysts with different PdO loadings ($\alpha = 5, 10, 13, 15, 20$).

**Table 5** PdO crystallite size, specific surface area, amount of oxygen desorption site and surface oxygen vacancy density of $\alpha$wt%PdO/16wt%Sr$_3$Fe$_2$O$_{7-\delta}$/$\alpha$-Al$_2$O$_3$ catalysts with different PdO loadings ($\alpha = 1, 3, 5, 10, 13, 15, 20$)

| Sample | PdO crystallite size/nm | Specific surface area/m$^2$ g$^{-1}$ |
|---|---|---|
| $\gamma$-Al$_2$O$_3$ | — | 148.0 |
| $\alpha$-Al$_2$O$_3$ | — | 14.6 |
| Sr$_3$Fe$_2$O$_7$ | — | 30.5 |
| 10wt%PdO/SrFeO$_{3-\delta}$ | 19.1 | 21.6 |
| 10wt%PdO/$\alpha$-Al$_2$O$_3$ | 3.7 | 2.5 |
| 16wt%Sr$_3$Fe$_2$O$_{7-\delta}$/$\alpha$-Al$_2$O$_3$ | — | 80.9 |
| 10wt%PdO/16wt%Sr$_3$Fe$_2$O$_{7-\delta}$/$\alpha$-Al$_2$O$_3$ | 9.2 | 70.2 |

smaller than crystallite size of PdO calculated from the XRD analysis results. These differences may be due to the aggregation of PdO in high concentration PdO supported $\alpha$wt%PdO/16wt%Sr$_3$Fe$_2$O$_{7-\delta}$/$\alpha$-Al$_2$O$_3$ catalysts. Additionally, EDS images (Fig. S8(a)†) confirm the homogeneous distribution of Pd, Sr, Fe, and Al elements, affirming the uniformity of the as-prepared catalyst samples. While Al elements are widely distributed, Sr, Fe, and Pd are locally and uniformly distributed. These results indicate that PdO and Sr$_3$Fe$_2$O$_{7-\delta}$ are effectively supported on surface of $\alpha$-Al$_2$O$_3$, with PdO expected to exist either in the form of PdO/Sr$_3$Fe$_2$O$_{7-\delta}$ or independently on the surface of Al$_2$O$_3$.[61-63]

Fig. 5(b) presents the O$_2$-TPD profile recorded on the $\alpha$wt%PdO/16wt%Sr$_3$Fe$_2$O$_{7-\delta}$/$\alpha$-Al$_2$O$_3$ catalysts ($5 \leq \alpha \leq 20$). When PdO was supported up to 13wt%, the oxygen desorption area continued to increase, and the desorption temperature decreased to around 100 °C of low temperature. The highest

oxygen desorption area was obtained at the sample of $\alpha = 13$ wt%. The increase of the oxygen desorption area can be explained by the production of oxygen vacancies on the crystal surface and within the lattice to maintain charge compensation, because Fe$^{4+}$ is reduced to Fe$^{3+}$ during CH$_4$ gas decomposition reaction. However, in range of $\alpha > 13$wt%, the amount of oxygen desorption decreased, and the desorption temperature increased. It can be inferred that the formation of oxygen vacancies can be suppressed by excessive aggregation of Pd metal in range of $\alpha > 13$wt% caused to reduce the property of electron donor. From this O$_2$-TPD analysis, the density of oxygen vacancy was estimated based on the desorption amount of O$_2$, as shown in Table 5. Among the prepared catalysts, 13wt%PdO/16wt%Sr$_3$Fe$_2$O$_{7-\delta}$/$\alpha$-Al$_2$O$_3$ catalysts showed the highest oxygen vacancy density of $31.71 \times 10^{17}$ site m$^{-2}$. We assessed the catalytic activity for methane combustion over the $\alpha$wt%PdO/16wt%Sr$_3$Fe$_2$O$_{7-\delta}$/$\alpha$-Al$_2$O$_3$ ($1 \leq \alpha \leq 20$) catalysts, and the results are presented in Fig. 6(a). The temperature required for complete methane combustion decreased to 300 °C with an increase in PdO loading to $\alpha = 13$. However, at higher PdO loadings ($\alpha \geq 15$), the temperature of complete methane combustion rose to 325 °C, and catalytic activity decreased due to PdO aggregation and a reduction in the catalysts' surface area. These findings confirmed that the optimal PdO loading for methane combustion is 13 wt%. To investigate the effect on the catalytic activity for methane combustion in more detail, we calculated the TOF and specific reaction rates for the methane conversion reaction, varying the loading amount of PdO and the density of oxygen vacancies. In Fig. 6(b), the correlations of the specific reaction rate ($r_{225°C}$) and the turnover frequency (TOF) to the density of PdO active sites at 275 °C for oxidation of methane for the various catalysts is presented. To isolate the effect of PdO loading, we normalized the TOF and the specific reaction rate at 225 °C with surface density and mass of PdO active site. Additionally, it was determined that the specific reaction rate and TOF also continuously increased as the oxygen vacancy density increased (Fig. 6(c)). The highest oxygen vacancy density and the fastest methane combustion rate were observed when the PdO loading amount was 13 wt%. The 13wt%PdO/16wt%Sr$_3$Fe$_2$O$_{7-\delta}$/$\alpha$-Al$_2$O$_3$ catalyst showed methane conversion of 100% at the lowest temperature of 300 °C. It can be determined that the highest oxygen vacancy density and surface oxygen species in the catalyst promoted methane combustion activity in combination with PdO active species. The catalyst recyclability test for methane combustion was performed using the 13wt%PdO/16wt%Sr$_3$Fe$_2$O$_{7-\delta}$/$\alpha$-Al$_2$O$_3$ catalyst and the results are shown in Fig. S9(a).† Although the methane combustion activity decreased slightly at some temperature with each iteration of methane combustion analysis, they are showed the same temperature of initial and complete methane combustion. From the XRD patterns of the samples after cycling test, no impurity phase corresponding to the decomposition of the Sr$_3$Fe$_2$O$_{7-\delta}$ catalyst was observed (Fig. S9(b)†). Additionally, the methane combustion activity of $\alpha$wt%PdO/16wt%Sr$_3$Fe$_2$O$_{7-\delta}$/$\alpha$-Al$_2$O$_3$ catalysts with low PdO loading amount ($\alpha = 1, 3$) under a methane concentration of 2.5% and mass hourly space velocity of 120 000 L kg$^{-1}$ h$^{-1}$ are

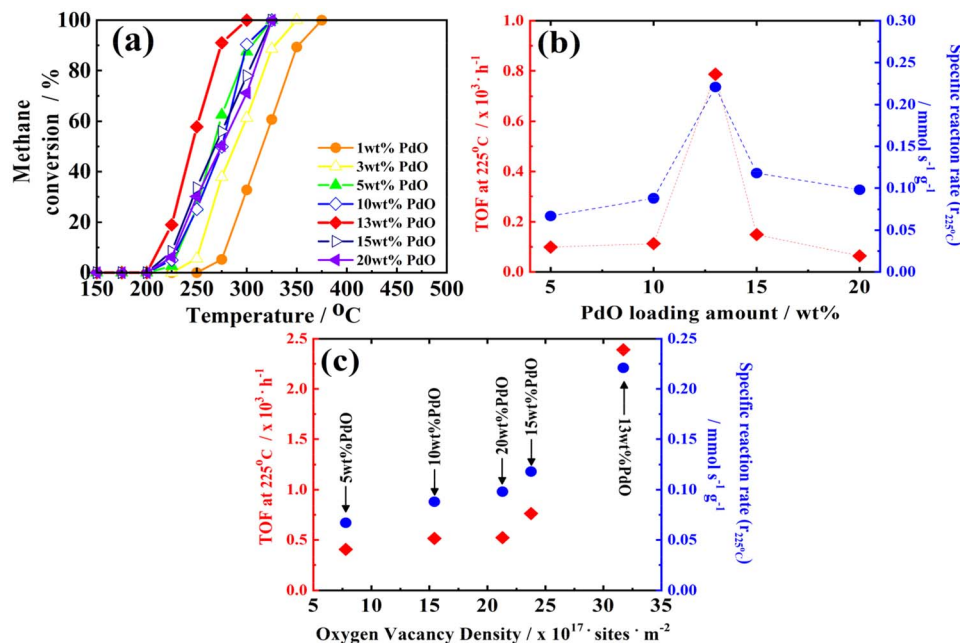**Fig. 6** (a) Temperature-dependence of methane oxidation over the α wt%PdO/16wt%Sr$_3$Fe$_2$O$_{7-\delta}$/α-Al$_2$O$_3$ catalysts with different PdO loadings (α = 1, 3, 5, 10, 13, 15, 20). (b) Correlations of the specific reaction rate (r$_{225°C}$) and the turnover frequency (TOF) to the density of PdO active sites at 225 °C for oxidation of methane over the αwt%PdO/16wt%Sr$_3$Fe$_2$O$_{7-\delta}$/α-Al$_2$O$_3$ catalysts (α = 5, 10, 13, 15, 20). (c) Correlations of the specific reaction rate and TOF to the density of oxygen vacancy estimated based on the amount of O$_2$ derived from the O$_2$-TPD analysis of the αwt%PdO/16wt%Sr$_3$Fe$_2$O$_{7-\delta}$/α-Al$_2$O$_3$ catalysts (α = 5, 10, 13, 15, 20).

shown in Fig. S9(c).† 1wt%PdO/16wt%Sr$_3$Fe$_2$O$_{7-\delta}$/α-Al$_2$O$_3$ catalyst did not show the complete methane combustion activity under 600 °C. On the other hand, 3wt%PdO/16wt%Sr$_3$Fe$_2$O$_{7-\delta}$/α-Al$_2$O$_3$ catalyst showed the complete methane combustion activity at 400 °C with $T_{50}$ of around 280 °C and $T_{90}$ of 350 °C. In similar methane concentration and PdO loading amount, the novel catalyst based on Sr$_3$Fe$_2$O$_{7-\delta}$ perovskite oxide prepared in this study showed superior methane combustion activity under low temperature compared to the reported catalyst.[64,65]

## Conclusions

We prepared PdO/Sr$_3$Fe$_2$O$_{7-\delta}$/α-Al$_2$O$_3$ composite oxide catalysts using a co-precipitation and impregnation method and assessed their catalytic performance in low-temperature methane combustion. Sr$_3$Fe$_2$O$_7$ perovskite oxide is known for its exceptional oxygen storage and release capabilities. However, to utilize it effectively in low-temperature methane oxidation, we needed to enhance its structural and thermal stability. This was essential to prevent the transformation of the Sr$_3$Fe$_2$O$_7$ perovskite structure, as it can change to SrFeO$_{3-\delta}$ when supporting PdO active species on Sr$_3$Fe$_2$O$_7$ oxide and calcining at 400 °C for 4 hours. In this study, we successfully synthesized αwt%PdO/16wt%Sr$_3$Fe$_2$O$_{7-\delta}$/α-Al$_2$O$_3$ composite oxide catalysts with Sr$_3$Fe$_2$O$_{7-\delta}$ as a co-catalyst. These catalysts formed only oxygen vacancies without distorting the crystal structure of Sr$_3$Fe$_2$O$_7$. By employing an α-Al$_2$O$_3$ support, we improved the thermal stability of the catalysts. The structural integrity remained intact even after heat treatment at 600 °C. Notably, the 16wt%Sr$_3$Fe$_2$O$_{7-\delta}$/α-Al$_2$O$_3$ co-catalyst, without PdO

active species, displayed no methane oxidation activity. In comparison, the 10wt%PdO/SrFeO$_{3-\delta}$ catalyst, lacking α-Al$_2$O$_3$ support, exhibited lower methane oxidation activity compared to 10wt%PdO/16wt%Sr$_3$Fe$_2$O$_{7-\delta}$/α-Al$_2$O$_3$. This comparison solidified the position of the composite oxide catalyst, comprising PdO/Sr$_3$Fe$_2$O$_{7-\delta}$/α-Al$_2$O$_3$, as the superior choice. It offered higher oxygen vacancy density and surface oxygen species, making it the most suitable catalyst for methane oxidation among various compositions. Finally, after optimizing the PdO loading, the 13wt%PdO/16wt%Sr$_3$Fe$_2$O$_{7-\delta}$/α-Al$_2$O$_3$ composite oxide catalyst achieved complete methane combustion at the remarkably low temperature of 300 °C, demonstrating the highest methane oxidation activity. Also, this study underscores the potential of this novel catalyst, where Sr$_3$Fe$_2$O$_{7-\delta}$ perovskite oxide plays a pivotal role as a promoter in methane combustion at low temperature even with low PdO loading amount of 3 wt%.

## Data availability

The datasets used and/or analysed during the current study for the article cannot be made available to recommended repositories due to legal confidentiality requirements for research data management plans (DMPs) of Funder guidelines.

## Author contributions

The manuscript was written through contributions of all authors. All authors have given approval to the final version of the manuscript.

## Conflicts of interest

There are no conflicts to declare.

## Acknowledgements

## References

1 H. Lin, Y. Liu, J. Deng, L. Jing and H. Dai, *Catalysts*, 2023, **13**(2), 427.

2 Y. Gao, M. Jiang, L. Yang, Z. Li, F. Tian and Y. He, *Front. Chem.*, 2022, **10**, 959422.

3 L. He, Y. Fan, J. Bellettre, J. Yue and L. Luo, *Front. Chem.*, 2020, **119**, 109589.

4 V. A. Likhanov and O. P. Lopatin, *Therm. Eng.*, 2017, **64**, 935–944.

5 T. Y. Kim, S. B. Jo, C. H. Lee, S. H. Kang, J. W. Kim, S. C. Lee and J. C. Kim, *Korean J. Chem. Eng.*, 2020, **37**, 1690–1698.

6 Y. S. Yu, X. W. Zhang, J. Liu, Y. Lee and X. S. Li, *Energy Environ. Sci.*, 2021, **14**, 5611–5668.

7 G. Zhao, X. Pan, Z. Zhang, Y. Liu and Y. Lu, *J. Catal.*, 2020, **384**, 122–135.

8 S. J. Yeo, J. S. Kim and W. J. Lee, *J. Cleaner Prod.*, 2021, **30**, 129955.

9 I. Tvedten, S. Bauer and J. Clean, *Energy Res. Soc. Sci.*, 2022, **86**, 102423.

10 B. Wang, S. A. Suazo, Y. P. Torres and E. Nikolla, *Catal. Today*, 2017, **285**, 147–158.

11 K. Murata, D. Kosuge, J. Ohyama, Y. Mahara, Y. Yamamoto, S. Arai and A. Satsuma, *ACS Catal.*, 2019, **10**, 1381–1387.

12 M. Cargnello, J. D. Jaén, J. H. Garrido, K. Bakhmutsky, T. Montini, J. C. Gámez, R. J. Gorte and P. Fornasiero, *Science*, 2012, **337**, 713–717.

13 P. Gélin and M. Primet, *Appl. Catal., B*, 2002, **39**, 1–37.

14 F. F. Tao, J. J. Shan, L. Nguyen, Z. Wang, S. Zhang, L. Zhang, Z. Wu, W. Huang, S. Zeng and P. Hu, *Nat. Commun.*, 2015, **6**, 7798.

15 G. Ercolino, P. Stelmachowski, G. Grzybek, A. Kotarba and S. Specchia, *Appl. Catal., B*, 2017, **206**, 712–725.

16 T. M. Onn, S. Zhang, L. Arroyo-Ramirez, Y. C. Chung, G. W. Graham, X. Pan and R. J. Gorte, *ACS Catal.*, 2015, **5**, 5696–5701.

17 X. Zou, Z. Rui and H. Ji, *ACS Catal.*, 2017, **7**, 1615–1625.

18 J. H. Park, J. H. Cho, Y. J. Kim, E. S. Kim, H. S. Han and C. H. Shin, *Appl. Catal., B*, 2014, **160–161**, 135–143.

19 H. Peng, C. Rao, N. Zhang, X. Wang, W. Liu, W. Mao, L. Han, P. Zhang and S. Dai, *Angew. Chem., Int. Ed.*, 2018, **57**, 8953–8957.

20 Q. Dai, Q. Zhu, Y. Lou and X. Wang, *J. Catal.*, 2018, **357**, 29–40.

21 A. R. Supandi, N. Nunotani and N. Imanaka, *J. Asian Ceram. Soc.*, 2020, **8**, 745.

22 P. G. Choi, N. Nunotani and N. Imanaka, *J. Asian Ceram. Soc.*, 2018, **6**, 368–373.

23 Y. B. Choi, N. Nunotani and N. Imanaka, *Mater. Lett.*, 2020, **278**(1–4), 128392.

24 Y. B. Choi, N. Nunotani, K. Morita and N. Imanaka, *J. Asian Ceram. Soc.*, 2022, **10**, 178.

25 Y. B. Choi, N. Nunotani, K. Morita and N. Imanaka, *Catalysts*, 2022, **12**, 69.

26 M. Jeong, N. Nunotani and N. Imanaka, *Bull. Chem. Soc. Jpn.*, 2018, **91**, 158.

27 Y. Ding, Y. Jia, M. Jiang, Y. Guo, L. Wang, Q. Ke, M. N. Ha, S. Dai and W. Zhan, *Chem. Eng. J.*, 2021, **416**, 129150.

28 M. Alyani and K. J. Smith, *Ind. Eng. Chem. Res.*, 2016, **55**, 8309–8318.

29 D. Ciuparu, M. R. Lyubovsky, E. Altman, L. D. Pfefferle and A. Datye, *Catal. Rev.:Sci. Eng.*, 2002, **44**, 593–649.

30 W. R. Schwartz, D. Ciuparu and L. D. Pfefferle, *J. Phys. Chem. C*, 2012, **116**, 8587–8593.

31 R. Gholami, M. Alyani and K. J. Smith, *Catalysts*, 2015, **5**, 561–594.

32 K. Persson, L. D. Pfefferle, W. Schwartz, A. Ersson and S. G. Jaras, *Appl. Catal., B*, 2007, **74**, 242–250.

33 S. J. Ramos, G. S. Dinali, C. Oliveira, G. C. Martins, C. G. Moreira, J. Siqueira and L. R. G. Guilherme, *Curr. Pollut. Rep.*, 2016, **2**, 28–50.

34 J. Wu, R. Ye, D. J. Xu, L. Wan, T. R. Reina, H. Sun, Y. Ni, Z. F. Zhou and X. Deng, *Front. Chem.*, 2022, **10**, 961355.

35 P. Zhang, Z. Lou, L. Gong, J. Xu, Q. Chen, M. J. Reece, H. Yan, Z. Dashevsky and F. Gao, *J. Alloys Compd.*, 2023, **937**, 168366.

36 P. Mars and D. W. van Krevelen, *Chem. Eng. Sci.*, 1954, **3**, 41–59.

37 L. He, Y. L. Fan, J. Bellettre, J. Yue and L. G. Luo, *Renewable Sustainable Energy Rev.*, 2020, **119**, 109589.

38 L. He, Y. L. Fan, F. C. Guo, K. R. Yang, J. A. Heinlein, S. M. Bamonte and J. J. Fee, *J. Am. Chem. Soc.*, 2020, **142**, 17119–17130.

39 F. Zasada, J. Janas, W. Piskorz, M. Gorczyńska and Z. Sojka, *ACS Catal.*, 2017, **7**, 2853–2867.

40 K. Beppu, S. Hosokawa, A. Demizu, Y. Oshino, K. Tamai, K. Kato, K. Wada, H. Asakura, K. Teramura and T. Tanaka, *J. Phys. Chem. C*, 2018, **21**, 11186–11193.

41 L. Peng, Q. Li, L. Sun and H. Zhao, *Catalysts*, 2021, **11**, 1400.

42 H. Falcon, J. A. Barbero, J. A. Alonso, M. J. Martınez-Lope and J. L. G. Fierro, *Chem. Mater.*, 2002, **14**, 2325–2333.

43 R. Bornovski, L. Huang, E. P. Komarala, J. M. Rondinelli and B. A. Rosen, *ACS Appl. Mater. Interfaces*, 2019, **11**, 33850–33858.

44 T. Akbay, A. Staykov, J. Druce, H. Téllez, T. Ishihara and J. A. Kilner, *J. Mater. Chem. A*, 2016, **4**, 13113–13124.

45 D. Halwidl, W. Mayr-Schmölzer, M. Setvin, D. Fobes, J. Peng, Z. Mao, M. Schmid, F. Mittendorfer, J. Redinger and U. A. Diebold, *J. Mater. Chem. A*, 2018, **6**, 5703–5713.

46 W. Tan, D. Huan, W. Yang, N. Shi, W. Wang, R. Peng, X. Wu and Y. A. Lu, *RSC Adv.*, 2018, **8**, 26448–26460.

47 B. Yang, X. Wu, B. K. Inusa, D. H. Kuo, P. Zhang, C. Li, T. Liu, D. Lu, Z. Yuan, J. Lin and X. Chen, *Chem. Eng. J.*, 2025, **514**, 163151.

48 X. Wu, T. L. Wan, B. Yang, D. H. Kuo, P. Zhang, M. Liu, S. N. Adawara, D. Lu, J. Lin and X. Chen, *J. Mater. Chem. A*, 2025, **13**, 17976.

49 Z. Su, B. Wu, C. Li, D. H. Kuo, P. Zhang, L. Chen, D. Lu, J. Lin, X. Chen and Z. Yuan, *Chem. Eng. J.*, 2025, **510**, 161621.

50 Y. Ling, F. Wang, R. A. Budiman, T. Nakamura and K. Amezawa, *Phys. Chem. Chem. Phys.*, 2015, **17**, 7489–7497.

51 Y. Ling, F. Wang, Y. Okamoto, T. Nakamura and K. Amezawa, *Solid State Ionics*, 2016, **288**, 298–302.

52 Z. Wang, W. Yang, S. P. Shafi, L. Bi, Z. Wang, R. Peng, C. Xia, W. Liu and Y. Lu, *J. Mater. Chem. A*, 2015, **3**, 8405–8412.

53 Y. Zhou, Z. Zhou, J. Sun, L. Liu, F. Luo, G. Xu, X. Cao and M. Xu, *EcoMat*, 2023, **5**, 12347.

54 K. Tamai, S. Hosokawa, H. Okamoto, H. Asakura, K. Teramura and T. Tanaka, *ACS Appl. Mater. Interfaces*, 2019, **11**, 26985–26993.

55 A. Takamatsu, K. Tamai, S. Hosokawa, T. Tanaka, M. Ehara and R. Fukuda, *ACS Appl. Mater. Interfaces*, 2021, **13**, 7216–7226.

56 K. Tamai, S. Hosokawa, K. Onishi, C. Watanabe, K. Kato, H. Asakura, K. Teramura and T. Tanaka, *ACS Catal.*, 2020, **10**, 2528–2537.

57 M. Jeong, N. Nunotani, N. Moriyama and N. Imanaka, *J. Asian Ceram. Soc.*, 2016, **4**, 259.

58 B. Wu, B. Yang, X. Wu, D. H. Kuo, Z. Su, L. Chen, P. Zhang, M. T. Mosisa, D. Lu, Z. Yuan, J. Lin and X. Chen, *ACS Appl. Mater. Interfaces*, 2024, **16**, 58764–58779.

59 Z. Su, B. Wu, D. H. Kuo, L. Chen, P. Zhang, B. Yang, D. Lu, J. Lin and X. Chen, *J. Mater. Chem. A*, 2024, **12**, 28486.

60 P. Zhang, L. Chen, D. H. Kuo, B. Wu, Z. Su, D. Lu, Q. Wu, J. Li, J. Lin and X. Chen, *J. Mater. Chem. A*, 2024, **12**, 7163.

61 X. Chen, T. Huang, D. H. Kuo, H. Sun, P. Li, O. A. Zelekew, A. B. Abdeta, Q. Wu, J. Zhang, Z. Yuan and J. Lin, *Appl. Catal., B*, 2021, **298**, 120542.

62 X. Chen, H. Sun, D. H. Kuo, A. B. Abdeta, O. A. Zelekew, Y. Guo, J. Zhang, Z. Yuan and J. Lin, *Appl. Catal., B*, 2021, **287**, 119992.

63 L. Chen, P. Zhang, D. H. Kuo, J. Jiang, B. Wu, Z. Su, O. A. Zelekew, J. Lin, D. Lu and X. Chen, *J. Mater. Chem. A*, 2024, **12**, 9871–9885.

64 Y. J. Zhang, J. R. Niu, G. Z. Wang, D. Li, H. X. Dai, H. He and W. G. Qiu, *J. Rare Earths*, 2006, **24**, 1–5.

65 Z. X. Wu, J. G. Deng, Y. X. Liu, S. H. Xie, Y. Jiang, X. T. Zhao, J. Yang, H. Arandiyan, G. S. Guo and H. X. Dai, *J. Catal.*, 2015, **332**, 13–24.